Journal of Rock Mechanics and Geotechnical Engineering 14 (2022) 477–493

Contents lists available at ScienceDirect

Journal of Rock Mechanics and Geotechnical Engineering

journal homepage: www.jrmge.cn

Full Length Article

Experimental and numerical investigation on the mechanical responses and cracking mechanism of 3D confined single-flawed rocks under dynamic loading

Wei You, Feng Dai, Yi Liu*

State Key Laboratory of Hydraulics and Mountain River Engineering, College of Water Resource and Hydropower, Sichuan University, Chengdu, 610065, China

ARTICLE INFO

Article history:
Received 28 February 2021
Received in revised form
16 July 2021
Accepted 9 September 2021
Available online 10 November 2021

Keywords:
Confined flawed rock
Split hopkinson pressure bar (SHPB)
Cracking mechanism
Discrete element method (DEM)

ABSTRACT

Accurately characterizing the mechanical responses and cracking mechanism of three-dimensional confined fractured rocks under coupled static-dynamic loading is of paramount importance for underground engineering construction. Using a modified split Hopkinson pressure bar (SHPB) system, five groups of single-flawed specimens with the axial prestress ratio from 0 to 0.8 are tested at the strain rates in the range of 65–205 s^{-1} under a fixed radial prestress. Our results indicate that both the dynamic strength and total strength show significant positive linear correlations with the strain rate, and the dynamic strength shows more strain rate sensitivity under higher axial prestress. The dynamic strength and corresponding failure strain decrease with increasing axial prestress, while the total strength is barely affected by the axial prestress. The dynamic elastic modulus initially increases before the axial prestress ratio reaches 0.6 and then decreases. The failure pattern of tested specimens changes from single diagonal failure to an "X" shaped conjugated failure as axial prestress increases. Furthermore, the progressive cracking processes of confined single-flawed specimens under different axial prestresses are numerically visualized by the discrete element method (DEM). Based on the displacement trend lines on both sides of cracking surface, five crack types are identified and classified in our simulation. The displacement field distributions of the DEM models reveal that the macroscopic single diagonal failure under lower axial prestress is mainly controlled by mixed tensile-shear cracks, while the "X" shaped conjugated failure under higher axial prestress is shear dominated.

1. Introduction

With the increasing demand for resources and spaces, a myriad of engineering structures are constructed in the deep underground, involving tunnel, hydropower house, nuclear waste repository, and oil depot (Jiang et al., 2021; Li et al., 2021). These underground rock structures are usually subjected to three-dimensional (3D) static in situ stress and dynamic disturbance simultaneously (Li et al., 2008; Liu and Dai, 2021), as depicted in Fig. 1. Widely existing in various underground structures, rocks containing many discontinuous flaws are generally in a triaxial stress state, and are extremely sensitive to coupled static-dynamic loading conditions (Zhao et al., 1999; Li et al., 2017a). It is thus crucial to investigate the dynamic response and cracking behaviors of 3D confined flawed rocks for the safety in the construction and operation of underground engineering.

Numerous studies about the flawed rocks were mainly concentrated on the static loading conditions (Wei et al., 2021). Under the uniaxial compression loading, rock specimens containing single flaw (Bobet and Einstein, 1998; Li et al., 2005), double flaws (Wong and Chau, 1998; Lee and Jeon, 2011; Shaunik and Singh, 2019) and even multiple flaws (Sagong and Bobet, 2002; Feng et al., 2018; Huang et al., 2019) were tested to investigate the mechanical properties and cracking behaviors. Results show that the strength and deformation characteristics of flawed rocks are significantly affected by the flaw geometric configuration, including the length and angle of the flaw, the length and angle of rock bridge, and the space between two flaws. Since rocks in practical engineering are generally confined by in situ stress in multiple directions, the effects of confining pressure on the static mechanical responses of flawed rocks were studied (Huang et al., 2016a, 2016b;

* Corresponding author.
E-mail address: liuyi_scu@163.com (Y. Liu).
Peer review under responsibility of Institute of Rock and Soil Mechanics, Chinese Academy of Sciences.

https://doi.org/10.1016/j.jrmge.2021.09.006

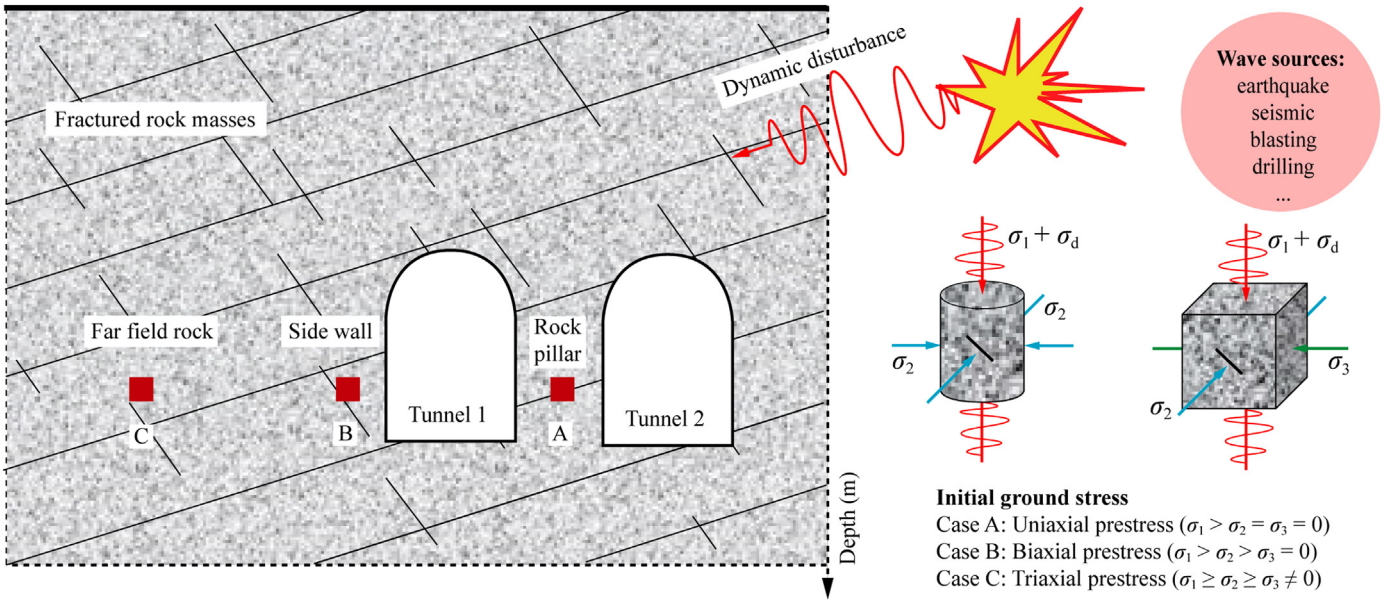

Fig. 1. The stress state of flawed rocks in underground engineering structure. σ_1, σ_2 and σ_3 are the major, intermediate and minor principal stresses, respectively; σ_d is the dynamic loading.

Tang et al., 2019). For example, Huang et al. (2016b) investigated the failure and internal damage behaviors of rock-like material specimens containing two un-parallel flaws using conventional triaxial compression tests. Results show that the crack evolution and failure mode are mainly affected by the fissure angle under lower confining pressure, while the effect of confining pressure becomes more significant under higher confining pressure.

Since the dynamic properties of rocks distinctly differ from that under static loading conditions, the dynamic characteristics of rocks at high strain rates have been further investigated using the split Hopkinson pressure bar (SHPB) apparatus (Frew et al., 2001; Dai et al., 2010; Xia and Yao, 2015; Xu et al., 2020). With increasing strain rate, the dynamic strength of rocks generally increases remarkably and the breakage degree of specimens turns serious. Recently, several dynamic loading tests have been conducted on the rocks containing different flaws (Zou and Wong, 2014; Li et al., 2017b, 2019). It is found that the flawed specimen usually shows a shear-dominated "X" shaped failure mode under individual dynamic loading, while the geometry of the flaws shows a little influence on the failure pattern. Meanwhile, a considerable number of researchers have investigated the coupled static-dynamic effect on the mechanical behaviors of intact specimens under one-dimensional (1D) or 3D stress conditions (Li et al., 2008; Gong et al., 2019; Pei et al., 2020; Liu et al., 2021). It is concluded that the coupled dynamic behaviors of rocks are influenced by both the initial prestress and dynamic loading rates. Nevertheless, the literature discussing the mechanical and cracking behaviors of the flawed rocks under coupled static-dynamic loading is rather limited (Yan et al., 2020, 2021; Xiao et al., 2020). Yan et al. (2020) reported that the failure modes of single-flawed specimens changed from a shear-dominated "X" shaped failure under individual dynamic loading to mixed shear-tensile failure under coupled static-dynamic loading. However, their study was limited in 1D prestress condition. So far, the dynamic behavior of 3D confined flawed rock under the coupled static-dynamic loading has never been investigated.

In this study, the sandstone specimen containing a prefabricated flaw is introduced into the coupled static-dynamic triaxial SHPB tests to investigate the effect of the axial prestress on the strength characteristics, deformation properties, failure pattern and cracking mechanism of the confined single-flawed rocks. After the laboratory tests, a numerical triaxial SHPB system is established by the open-source discrete element method (DEM) code, and the microscopic parameters of the DEM model are calibrated based on our experimental results. By the DEM simulations, the stress distribution, progressive cracking process and final displacement field are described for a further insight into the cracking mechanism of confined single-flawed specimens under coupled static-dynamic loading.

2. Experimental and numerical methodology

2.1. Testing apparatus and sealing process

As depicted in Fig. 2, the coupled static-dynamic tests on the confined single-flawed specimen are conducted in the modified SHPB experimental apparatus, which is mainly composed of bar system, pressure system and data acquisition system. The bar system is made of low-alloy ultrahigh strength steel, including a striker bar (300 mm in length), an incident bar (3000 mm in length) and a transmitted bar (2000 mm in length). The elastic modulus, density and diameter of these bars are 211 GPa, 7800 kg/m^3 and 50 mm, respectively. Two groups of strain gauges are mounted on appropriate positions of the incident bar and transmitted bar. Each group contains two strain gauges oppositely pasted on the circumferential surfaces of the bar. The pressure system includes a radial confining pressure system at the specimen and an axial confining pressure system at the end of the transmitted bar. Driven by the axial confining system, the axial prestress is exerted by the transmitted bar on the single-flawed specimen, while the radial prestress is applied by hydraulic oil in the chamber of radial confining system. Fig. 3a demonstrates the time histories of the radial confining pressure in different loading conditions. The maximum variation of radial confining pressure is lower than

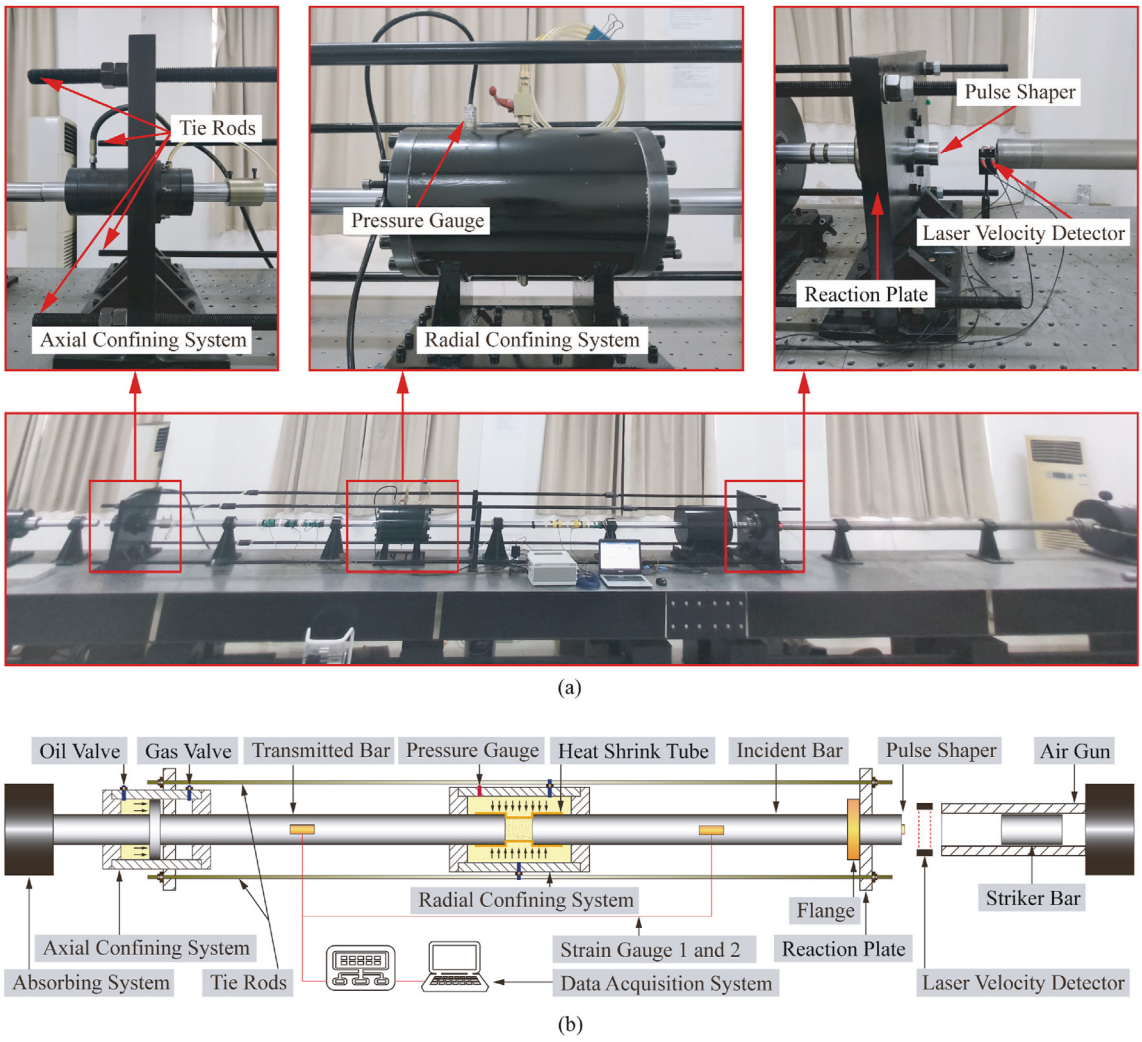

Fig. 2. (a) Photographs and (b) schematic diagram of the modified SHPB apparatus with radial and axial confining system.

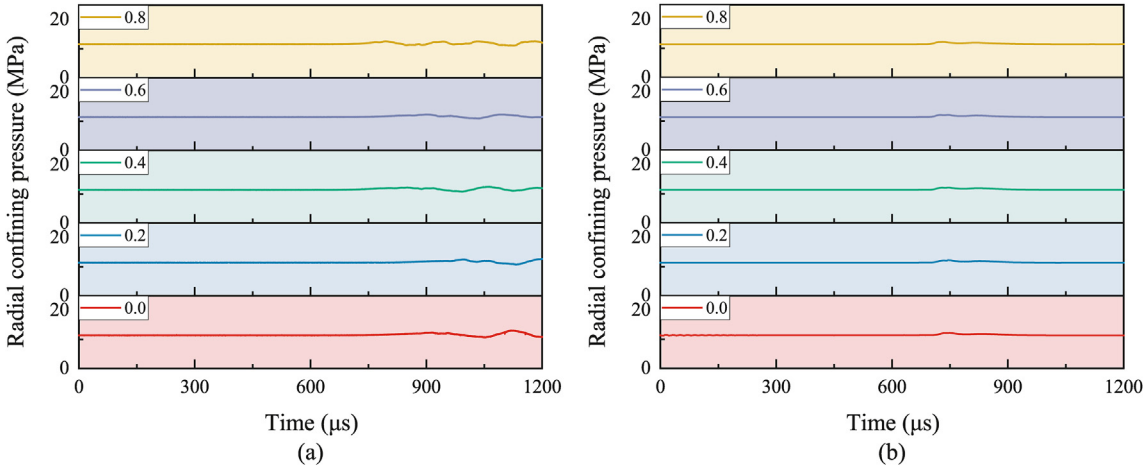

Fig. 3. Radial confining pressure variation in different axial prestress conditions: (a) Experiment and (b) Numerical simulation. The legends represent different axial prestress ratios.

1 MPa, indicating that the radial chamber is large enough to ensure the stability of confining pressure in the dynamic impact process.

If the single-flawed specimen was directly placed in the radial confining chamber to apply the confining pressures, high pressure

oil would fill the flaw and permeate the bar-specimen interfaces, which counteracts the confining pressure and hardly access the initial stress state of the rock. Therefore, the specimen should be well sealed between the incident and transmitted bars. The specific sealing process is shown in Fig. 4, mainly including five steps:

(1) Three O-shape rubber gaskets are set at the contact end between the specimen and each bar, respectively.
(2) With both ends lubricated by grease, rock specimens are sandwiched between the incident and transmitted bars and then wrapped by a heat shrink tube.
(3) After heating the heat shrink tube, steel hoops are tightened at the positions of rubber gaskets for sealing.
(4) The two ends of the heat shrink tube are coated with hot melt adhesive to prevent the high pressure oil from seeping through the heat shrink tube, which further ensures good sealing performance.
(5) Finally, a metal strainer is tied on the outside of the heat shrink tube to collect the fragments and residue of the rock specimen in case the heat shrink tube is punctured during the dynamic loading.

To prevent the high-pressure oil from penetrating the heat shrink tube through the preformed flaw, two high-strength alloy sheets are placed on the sidesurface of the single-flawed rock specimen with lubricating grease.

2.2. Specimen preparation and test scheme

The tested sandstone taken from Neijiang, Sichuan Province of China, which is homogenous without distinct defects and the average density is 2354 kg/m^3. A hydraulic servo-controlled MTS-793 rock testing system is used to determine the static mechanical properties of tested sandstone, including the uniaxial compressive strength (UCS) and indirect tensile strength. The basic physico-mechanical parameters of tested sandstone are listed in Table 1, in which the cylinder specimen with a diameter of 50 mm and an aspect ratio of 2:1 was used for calculating the UCS, and the Brazilian disc specimen with the geometry of 50 mm × 25 mm (diameter × thickness) was used for calculating the tensile strength.

Table 1
Basic physico-mechanical parameters of Neijiang sandstone.

Parameter	Unit	Value
Density, ρ	kg/m^3	2354
Young's modulus, E	GPa	6.7
Poisson's ratio, ν		0.23
UCS, σ_c	MPa	61
Brazilian tensile strength, σ_t	MPa	7

The geometry of cuboid sandstone specimens is 35 mm × 35 mm × 45 mm, as illustrated in Fig. 5a. A prefabricated flaw is located in the center of the specimen and the angle between the flaw and the loading direction is 45°. The fabrication process of the single flaw includes the following two steps. Firstly, a drilling bit is adopted to drill a small hole in the center of the specimen, and then a diamond wire saw with a thickness of 1 mm is passed through the hole to cut out a flaw with a length of 7 mm along the predetermined direction. After carefully polishing, all the specimens have a surface roughness less than 0.02 mm and the deviation of perpendicularity between two adjacent surfaces is smaller than 8′.

Fig. 5b briefly depicts the loading conditions of the single-flawed specimen in this study. For investigating the influence of axial prestress on dynamic response and cracking behaviors of flawed rock under 3D in situ stress, single-flawed specimens would be subjected to a fixed radial confining pressure and different axial prestress firstly, and then the dynamic pulse acts on the axial direction of rock specimen. The average UCS of single-flawed specimen is 56.8 MPa, and the radial confining pressure is fixed as 20% of the UCS (microcrack closure threshold) of single-flawed specimen, i.e. 11.4 MPa. Such level ground stress is commonly seen in the depth around 400–500 m where numerous engineering projects exist. In this study, the ratio of the static axial prestress to the

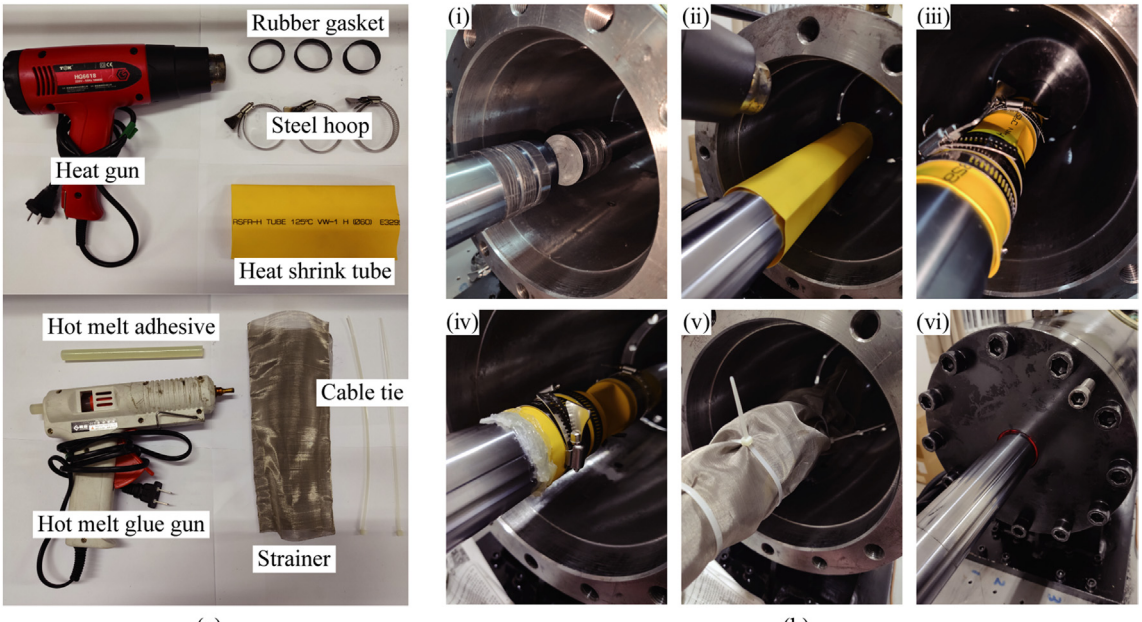

Fig. 4. (a) Sealing tools and (b) sealing process of the confined single-flawed rock specimen in coupled static-dynamic SHPB tests.

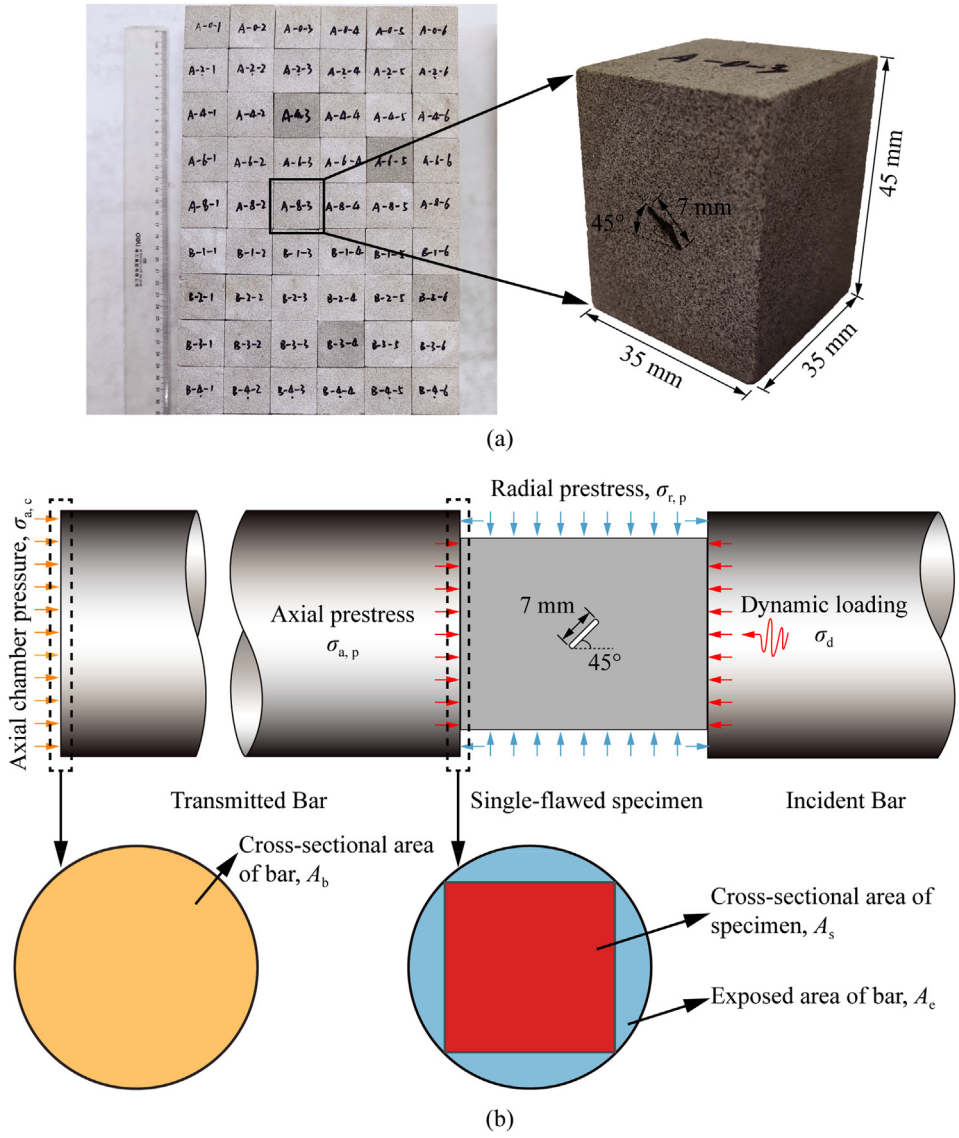

Fig. 5. (a) Geometrical parameters of the single-flawed specimen, and (b) the schematic loading conditions of the confined single-flawed specimen in coupled static-dynamic SHPB tests.

UCS of single-flawed specimen is defined as the axial prestress ratio. Five axial prestress ratios are selected to the confined single-flawed specimen, i.e. 0, 0.2, 0.4, 0.6 and 0.8, and thus the axial prestresses are set at 0 MPa, 11.4 MPa, 22.7 MPa, 34.1 MPa and 45.6 MPa, respectively. The specimens are divided into five groups based on different axial prestress ratios, and six specimens are tested in each group for different strain rates. Note that the applied radial prestress also acts on the exposed ends of the incident and transmitted bars, which reduces the designed axial prestress on the specimen. Therefore, to apply desired axial prestress on the specimen, the pressure in the axial confining chamber should be adjusted rather than make it equal to the axial prestress. Based on the force analysis of the transmitted bar at the static prestress stage, the following formula can be obtained:

$$\sigma_{a,\,c}A_b = \sigma_{a,\,p}A_s + \sigma_{r,\,p}A_e \tag{1}$$

where $\sigma_{a,\,c}$, $\sigma_{a,\,p}$ and $\sigma_{r,\,p}$ are the axial chamber pressure, axial prestress and radial prestress, respectively; A_b, A_s and A_e are the cross-sectional areas of bar and specimen, and the exposed area of bars, respectively. By transforming this formula, the pressure in axial confining chamber at different axial prestresses can be calculated as follows:

$$\sigma_{a,\,c} = \frac{\sigma_{a,\,p}A_s + \sigma_{r,\,p}A_e}{A_b} \tag{2}$$

Under different axial prestress ratios, the adjusted axial chamber pressures are 4.3 MPa, 11.4 MPa, 18.4 MPa, 25.5 MPa and 32.6 MPa, respectively.

2.3. Data acquisition and processing

When the designed axial and radial prestresses are achieved, the striker bar impacts upon the right end of incident bar and produces a comprehensive incident wave (ε_i). In order to obtain a ramp incident wave and facilitate the dynamic stress equilibrium state in the specimen, a red copper disk with dimensions of 10 mm × 2 mm (diameter × thickness) is glued on the right end of the incident bar

as a pulse shaper. When the incident wave propagates along the incident bar to the bar-specimen interface, part of the wave is reflected back as the reflected wave (ε_r), and the remainder goes through the specimen and travels into the transmitted bar as the transmitted wave (ε_t). All these strain signals are collected by the data acquisition system with a frequency of 10^7 s^{-1} during the dynamic tests.

In the coupled static-dynamic triaxial SHPB tests, there exists a detachment wave due to the separation between the reaction plate and flange (Chen et al., 2018). Data processing methods vary depending on whether the detachment wave arrives at the strain gauge after the reflected wave. With careful examination, the detachment wave passes through the strain gauge after the reflected wave in all tests of this study. Thus, the starting point of the reflected wave is zero. Meanwhile, affected by the axial constraint, the starting point of the incident wave and the transmitted wave is equal to the static axial prestress. Therefore, the dynamic stresses on the incident end (σ_i) and the transmitted end (σ_t) of the specimen can be calculated by the following equation:

$$\sigma_i = \frac{A_b}{A_s}E_b(\varepsilon_i+\varepsilon_r),\quad \sigma_t = \frac{A_b}{A_s}E_b\varepsilon_t \tag{3}$$

where E_b is the Young's modulus of the steel bars.

According to Chen et al. (2018) and Du et al. (2020a), the 1D stress wave theory by Kolsky (1949) is also applicable in coupled static-dynamic triaxial SHPB tests. Once the dynamic stress equilibrium is achieved during the loading process, i.e. $\sigma_i \approx \sigma_t$, the time-varying strain rate $\dot{\varepsilon}(t)$, dynamic strain $\varepsilon_{dyn}(t)$, and dynamic compressive stress $\sigma_{dyn}(t)$ of specimen can be calculated as follows:

$$\left.\begin{aligned}\dot{\varepsilon}(t) &= -\frac{2C_b}{l_s}\varepsilon_r(t)\\ \varepsilon_{dyn}(t) &= -\frac{2C_b}{l_s}\int_0^t \varepsilon_r(t)\mathrm{d}t\\ \sigma_{dyn}(t) &= \frac{A_bE_b}{A_s}[\varepsilon_t(t)-\varepsilon_{pre}]\end{aligned}\right\} \tag{4}$$

where C_b is the longitudinal wave velocity of the bar, ε_{pre} is the pre-strain caused by the axial prestress, and l_s is the length of specimen.

2.4. Brief introduction to DEM

To investigate the failure process and the cracking mechanism of the confined single-flawed specimen under coupled static-dynamic loading, the open-source DEM code ESyS-Particle (Weatherley et al., 2014) is employed to build up the whole triaxial SHPB system. In the simulation, the specimens and bars are modeled as collections of nonuniform-size spherical rigid particles. At the contact point, two adjacent particles are bonded together using a bond particle model (BPM) proposed by Potyondy and Cundall (2004). The BPM has been widely used to analyze the mechanical behavior of rock materials (Xu et al., 2016; Liu et al., 2017; Du et al., 2020b; You et al., 2021). The forces and moments between bonded particles can be calculated using the following equation:

$$\left.\begin{aligned}F_{bn} &= k_{bn}\Delta d_n\\ F_{bs} &= k_{bs}\Delta d_s\\ M_b &= k_b\Delta\alpha_b\\ M_t &= k_t\Delta\alpha_t\end{aligned}\right\} \tag{5}$$

where F_{bn}, F_{bs}, M_b and M_t are the normal bond force, shear bond force, bending moment and twisting moment, respectively; k_{bn}, k_{bs}, k_b and k_t denote the normal, shear, bonding and twisting stiffnesses of bond, respectively; and Δd_n, Δd_s, $\Delta\alpha_b$ and $\Delta\alpha_t$ are the corresponding relative displacements. The criterion of BPM breakage is as follows:

$$\frac{F_{bn}}{F_{bn,\,max}}+\frac{F_{bs}}{F_{bs,\,max}}+\frac{M_b}{M_{b,\,max}}+\frac{M_t}{M_{t,\,max}}\geq 1 \tag{6}$$

where the subscript max denotes the maximum value of the corresponding force.

3. Experimental results

3.1. Dynamic stress equilibrium

The dynamic stress equilibrium on both ends of the specimen is a prerequisite for the quasi-static data analysis method in SHPB tests (Zhou et al., 2012; Xia and Yao, 2015). In our tests, the pulse shaping technique is employed to produce a ramp impact wave with a duration of about 300 μs, which provides enough time for wave reverberation in the specimen to achieve a dynamic stress equilibrium state. Fig. 6 demonstrates time-varying stresses on the two ends of the single-flawed specimens with confining pressure of 11.4 MPa under five typical axial prestress ratios of 0, 0.2, 0.4, 0.6 and 0.8, respectively. Due to the existence of the axial prestress, the starting point of the incident and transmitted waves is equal to corresponding axial prestress. The dynamic stress on the incident end is the sum of the incident and transmitted waves, marked as In + Re, while the dynamic stress on the transmitted end of the specimen is expressed by the transmitted wave, noted as Tr. At the beginning of dynamic loading, the incident stress (In + Re) is generally greater than the transmitted stress (Tr). After several wave reverberations, the dynamic stresses on two ends of the specimen are almost identical, which means that the dynamic stress equilibrium of the single-flawed specimen is well achieved in our coupled static-dynamic tests. The analysis in the following is based on the results of valid SHPB tests.

After the dynamic stress equilibrium is achieved, the time-varying strain rate and dynamic stress are obtained by Eq. (4). The evolutions of the strain rate $\dot{\varepsilon}(t)$ and dynamic stress $\sigma_{dyn}(t)$ in a typical test are presented in Fig. 7a. In the vicinity of the peak stress, it is clear that there exists a flat plateau in the time-strain rate curve during 171 μs and 204 μs, which indicates that the specimen is axially deformed at a constant speed. The strain rate is defined as the average value of the plateau. Fig. 7b depicts the dynamic stress-strain curve of the specimen. The peak value of the dynamic stress history is defined as the dynamic strength (σ_d) of the confined single-flawed specimens, and the corresponding dynamic strain is set as the dynamic failure strain (ε_{df}). Note that this stress-strain curve only exhibits the dynamic loading part while excluding the static pre-loading part. The slope of the dynamic stress-strain curve at the liner increasing stage is defined as the dynamic elastic modulus (E_d).

3.2. Strain rate effect on strength characteristics

The mechanical properties, including the dynamic strength, total strength, dynamic elastic modulus and dynamic failure strain of all tested specimens, are listed in Table 2. Note that the total strength for each confined specimen is the sum of the corresponding axial prestress and dynamic strength. In our tests, the strain rates of the specimens are distributed between 65 s^{-1} and 205 s^{-1} in different axial prestress groups. Fig. 8a and b depicts the strain rate effects on the dynamic strength and total strength of single-flawed specimens under different axial prestress ratios,

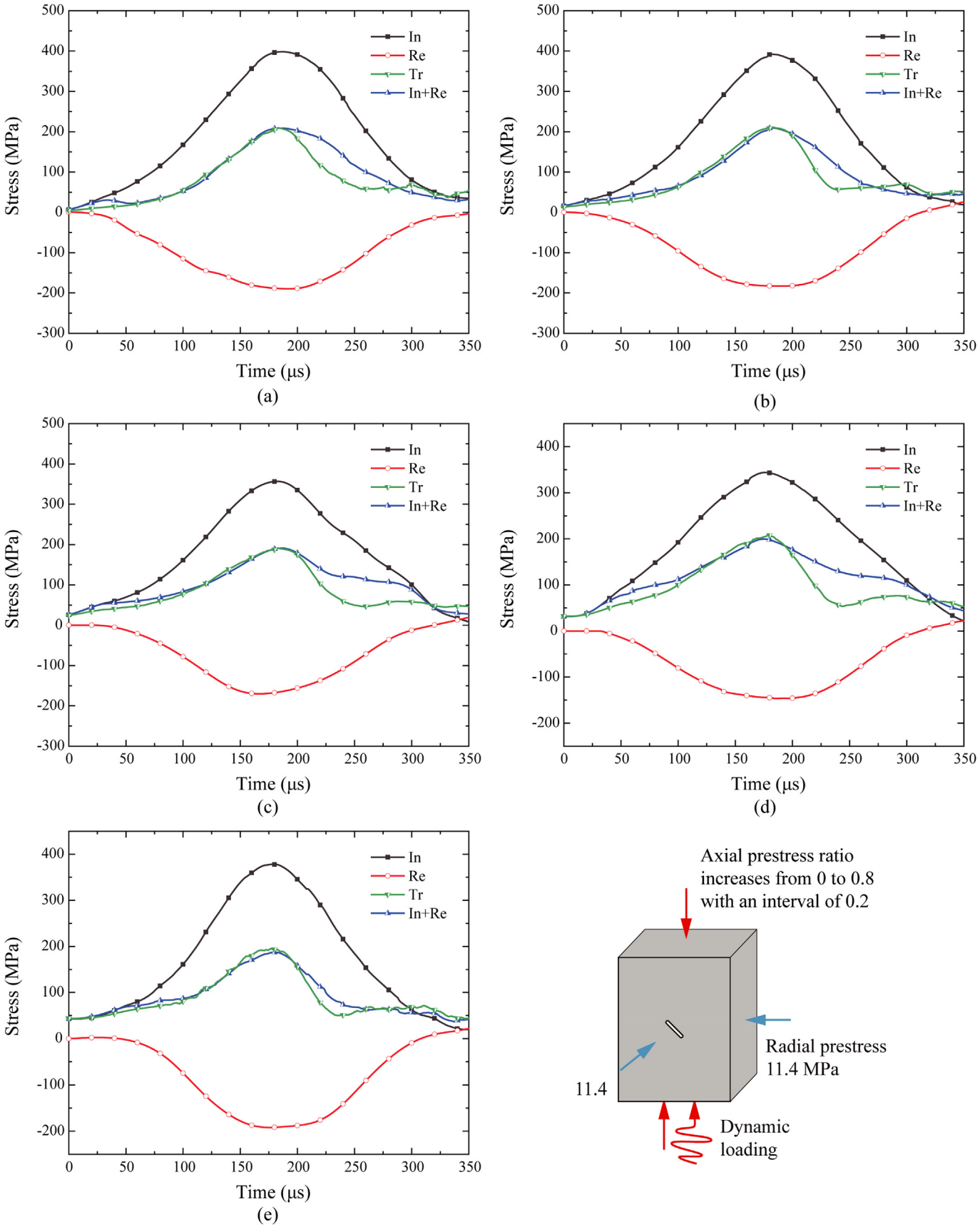

Fig. 6. Dynamic stress balance check of the confined single-flawed specimens under the axial prestress ratios of (a) 0, (b) 0.2, (c) 0.4, (d) 0.6 and (e) 0.8. In, Re and Tr represent the incident, reflected and transmitted stress waves, respectively.

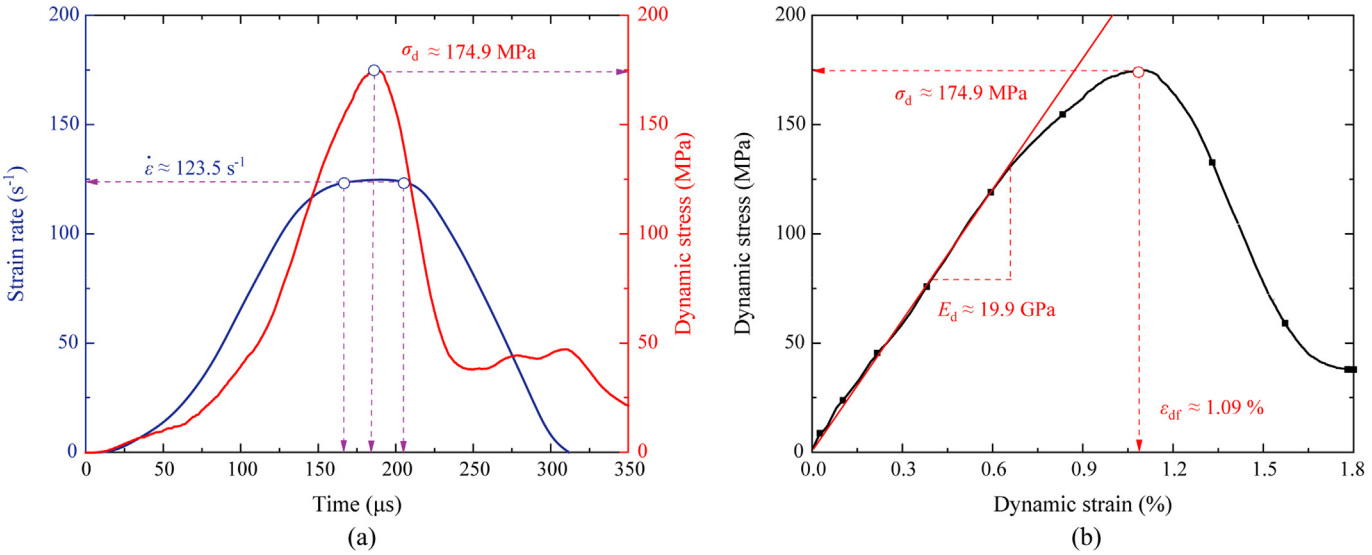

Fig. 7. Typical test data in coupled static-dynamic triaxial SHPB tests: (a) Evolutions of strain rate and dynamic stress, and (b) Dynamic stress–strain curve.

Table 2
Mechanical properties of the confined single-flawed specimens in coupled static-dynamic SHPB tests.

Specimen No.	Axial prestress (MPa)	Strain rate (s^{-1})	Dynamic strength (MPa)	Total strength (MPa)	Dynamic elastic modulus (GPa)	Dynamic failure strain (%)
A-0-3	0	67.5	171.6	171.6	20.5	1.03
A-0-5	0	95.5	173.5	173.5	13.9	1.11
A-0-2	0	125.2	183	183	14.7	1.26
A-0-1	0	166.4	191.7	191.7	17.1	1.39
A-0-6	0	188.0	196	196	20.2	1.69
A-0-4	0	204.3	203.7	203.7	19.3	1.63
A-2-3	11.4	100.4	169	180.4	17.1	1
A-2-2	11.4	123.5	174.9	186.3	19.9	1.09
A-2-1	11.4	146.4	180.6	192	11.2	1.22
A-2-5	11.4	160.6	188.9	200.3	20.4	1.21
A-2-6	11.4	178.9	195.6	207	16.5	1.52
A-2-4	11.4	203.9	208.8	220.2	18.3	1.81
A-4-5	22.7	94.7	153.8	176.5	17.5	0.95
A-4-4	22.7	110.7	158.3	181	17.4	1.03
A-4-6	22.7	124.1	162.8	185.5	18.6	1.02
A-4-2	22.7	137.4	167.3	190	19.5	1.06
A-4-3	22.7	153.2	171.8	194.5	21	1.16
A-4-1	22.7	161.2	179.4	202.1	20.4	1.19
A-6-2	34.1	69.7	141.3	175.4	24.1	0.77
A-6-1	34.1	92.1	152.2	186.3	13.9	0.76
A-6-3	34.1	122.8	155.7	189.8	20.9	0.9
A-6-4	34.1	137.8	156.4	190.5	16.6	0.93
A-6-6	34.1	153.8	165.1	199.2	24.2	1.22
A-6-5	34.1	161.7	170.2	204.3	22.1	1.27
A-8-5	45.4	87.9	123	168.4	16.8	0.7
A-8-6	45.4	106.8	136.4	181.8	17.2	0.93
A-8-4	45.4	123.4	143.4	188.8	20.2	0.81
A-8-2	45.4	143.9	146.3	191.7	18.3	0.97
A-8-3	45.4	154.7	156.7	202.1	17.1	1.06
A-8-1	45.4	170.1	181.4	226.8	20.7	1.11

respectively. At a given axial prestress ratio, the dynamic strength shows high rate dependence and increases with the rising of the strain rate. The final failure of rock is caused by the initiation, propagation and interaction of microcracks. From the perspective of energy, more microcracks are active in rock with the increase of strain rate, and more energy is thus consumed for crack generation in a short time. In this case, more micro-structures in rock specimens are involved in the resistance to damage, leading to the increase in macro-strength of rocks. The positive linear rate dependence of the total strength is also distinct under different axial prestress ratios.

It is observed that the increasing rate of dynamic strength under higher axial prestress ratio is faster than that under lower axial prestress ratio. Due to compaction of the radial confining pressure, most microcracks in rock specimen are closed. With the increasing axial prestress, however, more and more microcracks open again, and these open microcracks provide abundant reflected surfaces for the stress wave, leading to higher local damage in rocks. In this case, just a small dynamic strain rate could lead the failure of specimen, and the dynamic strength is thus more sensitive with strain rate under higher axial prestresses. Additionally, the superposition of axial static prestress and dynamic strength reduces the dispersion of total strength. Though under different axial prestress ratios, the distribution of total strength is closer and most data are gathered near a fit line (excluding specimen No. A-8-1), quite different from the relatively dispersed distribution of dynamic strength. Under the similar strain rate, the influence of axial prestress on dynamic strength is much greater than that on total strength. For example, at the strain rate about 123 s^{-1}, the maximum difference of dynamic strength is 39.6 MPa, while that of total strength is only 6.8 MPa.

3.3. *Influence of axial prestress on mechanical and deformation behaviors of single-flawed sandstone*

In order to further investigate the influence of the axial prestress on the strength characteristics, the dynamic strength and total strength of single-flawed specimens with confining pressure of 11.4 MPa are plotted against the axial prestress ratio in Fig. 9a and b, respectively. The strain rate is represented by the rainbow color. It can be found from Fig. 9a that there is a marked drop in dynamic strength as the axial prestress ratio increases from 0 to 0.8, indicating that the axial prestress weakens the dynamic bearing capacity of rock specimens. However, the total strength of tested specimen shows little sensitivity to the axial prestress (Fig. 9b). Compared with the specimens without axial preload, the total strength of specimens with axial preload is slightly increased. When the axial prestress ratio increases from 0.2 to 0.8, the total strength remains steady with little fluctuations. Compacted by

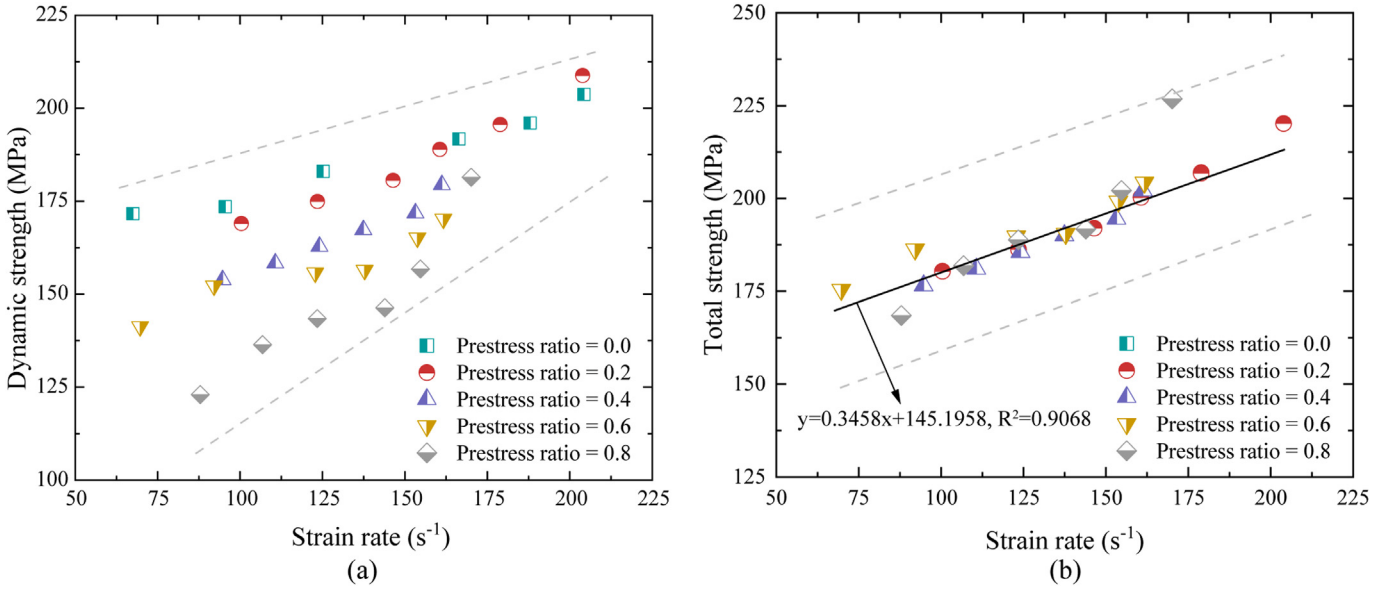

Fig. 8. (a) Dynamic strength and (b) total strength versus strain rate of the confined single-flawed specimens in coupled static-dynamic SHPB tests.

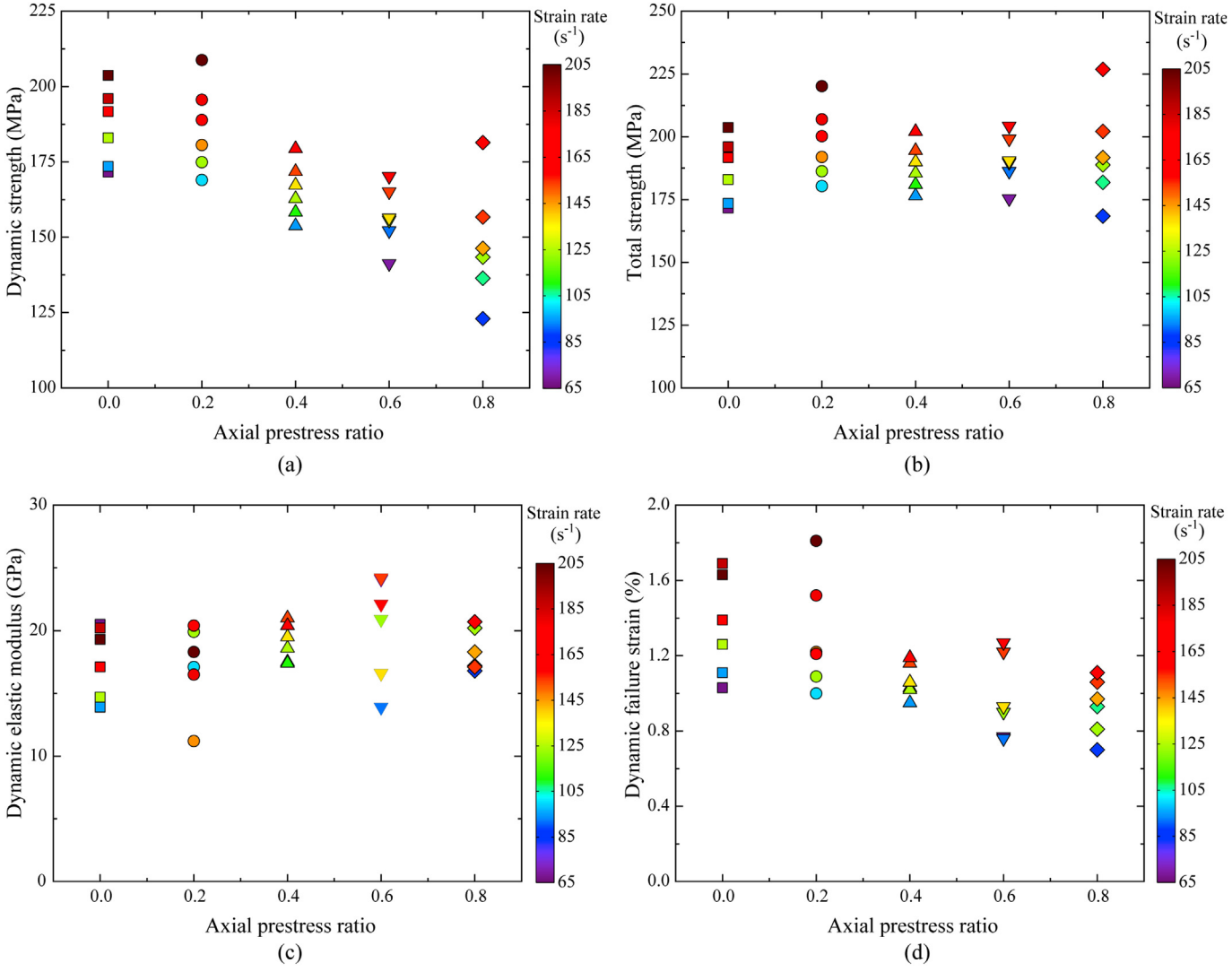

Fig. 9. Influence of axial prestress on mechanical and deformation behavior of the confined single-flawed specimen: (a) Dynamic strength, (b) Total strength, (c) Dynamic elastic modulus, and (d) Dynamic failure strain.

radial confining pressure, the rock specimen exhibits higher ductility. According to the maximum shear stress theory, the total axial yield point of rock is stable under the same radial stress environment, thus the higher the static axial prestress, the lower the dynamic bearing capacity under similar loading rate. Similar testing results were reported by Wu et al. (2015) about the dynamic tensile behavior of rocks under static pre-tension.

For characterizing the deformation behavior, Fig. 9c and d depicts the influence of axial prestress on the dynamic elastic modulus and dynamic failure strain, respectively. The dynamic elastic modulus first shows an increasing trend as the prestress ratio increases from 0 to 0.6, and then decreases at the ratio of 0.8, which probably because the microcracks gradually close and the porosity of specimen is decreasing when the axial prestress ratio is less than a critical level (around 0.6 in this study). While, as the axial prestress ratio surpasses the critical value, the closed microcracks are activated again and even extended. In addition, the dynamic failure strain in Fig. 9d presents a declining trend with increasing axial prestress under a similar strain rate, which is the same as the effect of axial prestress on the dynamic strength.

3.4. Failure pattern of single-flawed sandstone under different axial prestresses

The failure pattern analysis is an important method to learn the cracking mechanism of rocks. To reveal the effect of the axial prestress, the failure pattern of confined single-flawed specimens under the strain rate of about 122 s^{-1} is carefully examined, as depicted in Fig. 10. It can be observed that the failure modes of tested specimens are quite different as the axial prestress ratio increases from 0 to 0.8.

According to the crack types classification proposed by Li et al. (2017b), four basic crack types of single-flawed specimen are observed in this study, including coplanar shear (CS) crack, oblique shear (OS) crack, mixed shear-tensile (MST) crack, and far-field shear (FS) crack. Under lower axial prestress (i.e. the prestress ratios of 0 and 0.2), the OS or MST cracks coalesce with the FS cracks, forming two noncoplanar shear bands with pulverized rock powder. Therefore, the specimens generally exhibit a macroscopic diagonal failure pattern and broke into two major fragments. Under higher axial prestress (i.e. the prestress ratios between 0.4 and 0.8), accompanied by a series of FS and OS cracks, the CS cracks extend on another diagonal plane, which makes the failure pattern convert into an "X" shaped conjugated failure mode. Usually, four major fragments are formed after failure.

From the above analysis, the axial prestress appears a significant influence on the failure pattern of the confined single-flawed specimen. The failure mode changes from macroscopic diagonal failure for lower axial prestress to an "X" shaped conjugated failure for higher axial prestress. On the other hand, almost all crack types are shear cracks, and the tensile cracks are barely observed in our tests, which indicates that the failure mode is shear-dominated for the confined single-flawed specimens under coupled static-dynamic loading.

4. Numerical results

For further revealing the cracking mechanism of the confined single-flawed specimen under coupled static-dynamic loading, the numerical triaxial SHPB tests are conducted by the DEM simulation. With the aid of a self-compiled monitoring program, the invisible mechanical behavior of rocks in the laboratory tests can be obtained and visualized, including the stress distribution, crack propagation and final displacement field. The simulation results are exhibited and discussed in this section.

4.1. Model setup and micro-parameters calibration

As shown in Fig. 11, the numerical coupled static-dynamic triaxial SHPB system mainly consists of 3 bars (i.e. a striker bar, an incident bar and a transmitted bar), a pulse shaper and four lateral servo walls. The geometric sizes of these 3 bars in DEM model are the same as the realistic experimental SHPB apparatus mentioned in Section 2.1. Meanwhile, five measuring spheres are placed at Points A-E to record the propagating process of the stress waves. The single-flawed specimen is created by the following two steps. First, the particles assemble in a domain with the size of 35 mm × 35 mm × 45 mm to generate an intact specimen with bonds; then the particles in the designed flaw region are deleted. To obtain reliable mechanical properties and failure behavior of rock, a

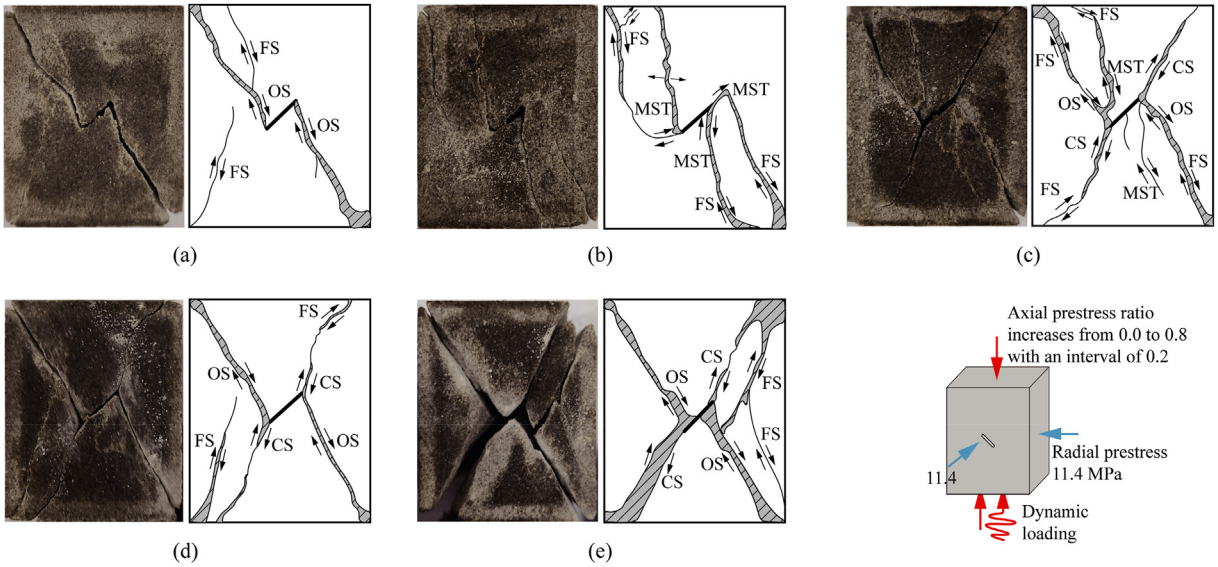

Fig. 10. The typical failure patterns of the confined single-flawed specimens at the axial prestress ratios of (a) 0, (b) 0.2, (c) 0.4, (d) 0.6, and (e) 0.8 in coupled static-dynamic SHPB tests. CS - coplanar shear crack; OS - oblique shear crack; MST - mixed shear-tensile crack; FS - far-field shear crack.

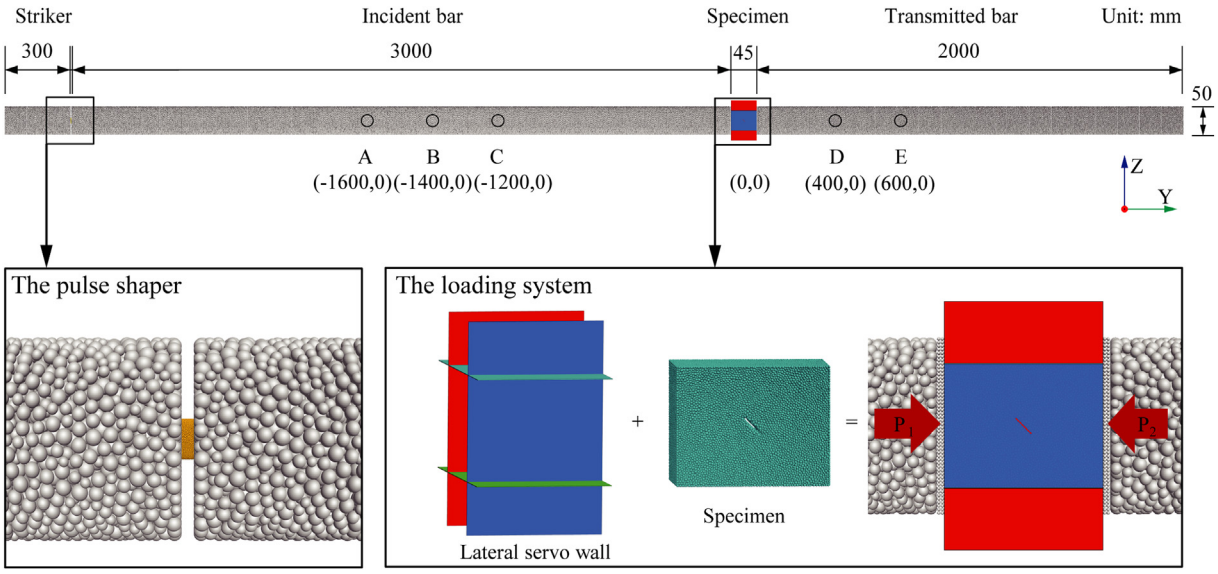

Fig. 11. The 3D discrete element model of the coupled static-dynamic triaxial SHPB system and the single-flawed specimen.

sufficiently small particle diameter must be set for the numerical specimen. Ding et al. (2014) carefully analyzed the particle size effects on the simulation results, and recommended that the ratio of the minimum dimension of the specimen to the average particle diameter is at least 25. In our simulation, the particle radius of specimen follows the uniform distribution $r_{max}/r_{min} = 1.66$ with $r_{min} = 0.26$ mm, where r_{max} and r_{min} are the maximum and minimum radii of the particles, respectively. Therefore, the ratio of the thickness of the specimen to the average particle diameter is about 50, which is large enough to eliminate the particle size effects on the simulation results.

The axial prestress is directly applied to the numerical single-flawed specimen by driving the incident and transmitted bars with a small displacement increment of 0.05 m/s. To dissipate the energy induced by applying the prestress, high damping is set in the simulated bars. Before the dynamic loading, the damping of bars is set as zero. In addition, four orthogonal rectangular walls form a lateral confining chamber to apply radial prestress on the specimen. Sufficient stiffness is allocated to these walls to simulate the high radial hydraulic pressure on the specimen (Weatherley et al., 2014; Du et al., 2020b). To ensure stable radial pressure in the dynamic loading process, an adaptive controller factor (G) is introduced to control the shrinkage of the servo wall. The relation between vertex velocity v_w of servo wall and the stress difference $\Delta\sigma$ can be expressed as follows:

$$v_w = G(\sigma_m - \sigma_p) = G\Delta\sigma \tag{7}$$

where σ_m and σ_p represent the measurement and predetermined lateral stresses, respectively. The controller factor G can be calculated as follows:

$$G = \frac{\alpha A_w}{k_n^{ave} N_c \Delta t} \tag{8}$$

where α is a relaxation parameter generally set as 0.5 in DEM simulations; A_w denotes the lateral servo wall area contacted with specimen; k_n^{ave} and N_c are the average normal stiffness and total number of all contacts between the wall and specimen, respectively; and Δt is the duration of each calculation step and automatically determined according to the scale of the whole model. All the lateral confinement variations of each axial prestress ratio group are negligible in the simulated dynamic loading process, as depicted in Fig. 3b.

By varying the microscopic parameters of the single-flawed specimen, a series of trial and error tests is performed to achieve a good agreement between numerical results and experimental results. In the calibration process, the static uniaxial compression tests are first simulated to acquire the designed elastic modulus and Poisson's ratio of rock specimen (macro), which is controlled by elastic modulus of particles and effective modulus and stiffness ratio of BPM model (micro). Secondly, the dynamic strength (macro) is matched by changing the bond cohesion parameter (micro) of BPM in the triaxial dynamic tests. The calibrated microscopic parameters of DEM model are listed in Table 3. The bond strength of simulated bars is set to a sufficiently large value because the steel bars never break in the common experiments (Xu et al., 2016, 2020; Du et al., 2020b). To examine the representative of the selected microscopic parameters, the comparison of numerical and experimental dynamic stress-strain curves under different axial prestress ratios with the similar strain rate is shown in Fig. 12a. It can be seen that the numerical and experimental curves exhibit well consistency in the region before the peak stress, though the DEM models are more brittle after the peak. The peak stresses (i.e. dynamic strength) of the DEM models are also in good agreement with the experiment results. In addition, the failure pattern of numerical specimen is similar to the laboratory results.

Table 3
Microscopic parameters of the numerical SHPB model.

Component	Microscopic parameter	Value	
		Specimen	SHPB bars
Particles	Radius (mm)	0.26–0.43	1.35–2.24
	Density (kg/m^3)	3923.3	12,582.1
	Elastic modulus (GPa)	16.5	300
	Stiffness ratio, k_n/k_s	2.5	2.5
	Friction coefficient	0.5	0.5
Bonds	Effective modulus (GPa)	18.5	300
	Stiffness ratio, k_n/k_s	2.5	2.5
	Tensile strength (MPa)	50 ± 5	1×10^{100}
	Shear strength (MPa)	60 ± 6	1×10^{100}
	Friction angle (°)	30	30

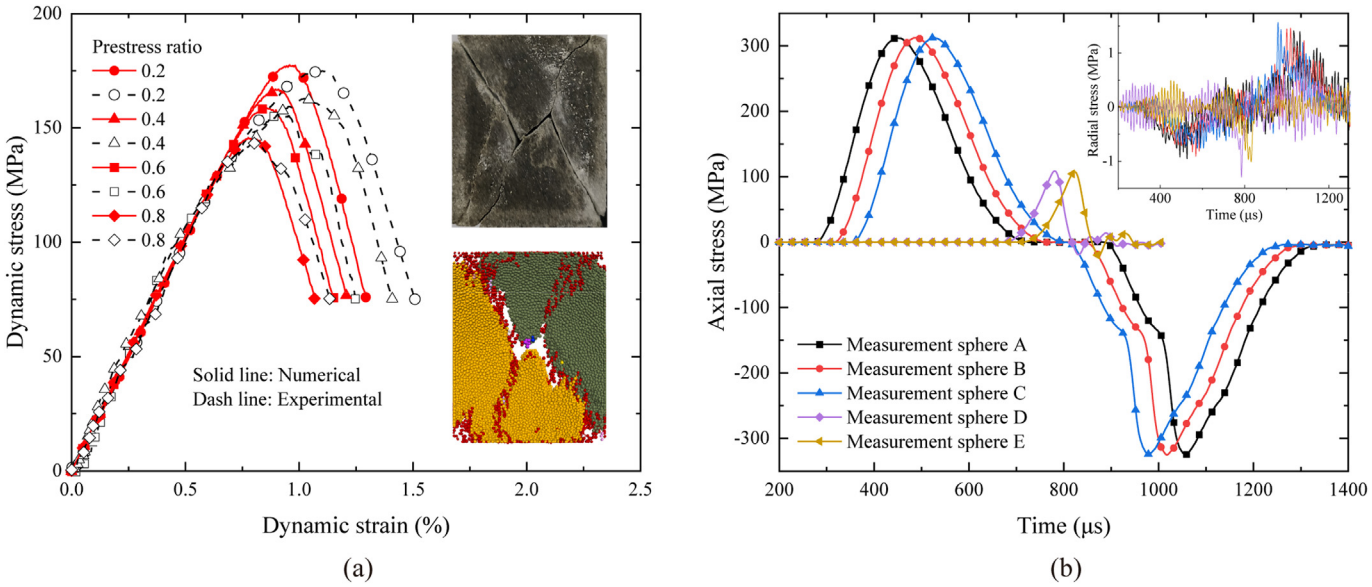

Fig. 12. (a) Comparisons of dynamic stress-strain curves and failure patterns between experimental and numerical results, and (b) axial and radial stress histories monitored by the measuring spheres (A–E) in our simulation under the axial prestress ratio of 0.6 and strain rate of about 122 s^{-1}.

For example, under axial prestress ratio of 0.6, both of them present an "X" shaped conjugated failure pattern. These consistent results guarantee that the selected microscopic parameters in our DEM models are appropriate to reproduce the mechanical and failure characteristics of the confined single-flawed rock specimens subjected to coupled static-dynamic loading.

In order to validate the numerical triaxial SHPB system, it is necessary to check whether two basic hypotheses are satisfied, i.e. the 1D stress propagation of bars and the dynamic stress equilibrium state of specimens. Fig. 12b displays the axial and radial stress signals in the incident and transmitted bars under the axial prestress ratio of 0.6 and strain rate of about 122 s^{-1}. For the axial stress, it can be clearly seen that these stress waves recorded at different positions in these 2 bars are almost identical in both the amplitudes and the waveforms. For the radial stress, the maximum amplitude of all radial stresses is only about 1.5 MPa, which is negligible compared with that of axial stress. These results indicate that the wave propagation attenuation and dispersion are not significant. Therefore, the 1D stress wave propagation assumption is verified in the numerical triaxial SHPB system.

For checking the dynamic stress equilibrium assumption, the stresses on the incident end and the transmitted end of the specimen are directly computed by monitoring the contact forces between the specimen and the bars. For example, Fig. 13 shows the axial dynamic stress on both ends of the specimen under the axial prestress ratios of 0.2 and 0.8, respectively. A stress equilibrium coefficient μ is used to assess the stress balance level of the specimen (Hokka et al., 2016; Du et al., 2020b):

$$\mu = \frac{2(\sigma_i - \sigma_t)}{\sigma_i + \sigma_t} \tag{9}$$

Four typical moments are also marked in Fig. 13, including T_b, T_f, T_p and T_e representing balanced, fracturing, peak and ending times of the cubic specimen failure process, respectively. T_b is the moment when μ is less than 10% for the first time, while T_e is the moment when μ is higher than 10% after T_b. T_f and T_p are the moments when the dynamic stress of specimen reaches 85% and 100% peak value, respectively. Between T_b and T_e, the stress equilibrium coefficient oscillates around zero with small amplitudes, which suggests that the dynamic stress balance level is acceptable in the DEM simulation.

4.2. Cracking process and stress field evolution

The dynamic stress field evolution and progressive cracking process are visualized to investigate the effect of axial prestress on rock failure behavior. In the view of the direction perpendicular to the dynamic loading, three slices with a thickness of 1 mm and an interval of 15 mm are shown to demonstrate the stress and crack changes at the center and surface of the specimens. The slice II is at the center, while the slices I and III are at the external position of the single-flawed specimen. The specific location of slices I–III is schematically depicted in Fig. 14. For comparison, under the radial prestress of 11.4 MPa, two typical tests, i.e. the axial prestress ratios of 0.2 and 0.8 under the strain rate of about 160 s^{-1}, are selected, and corresponding results are shown in Figs. 15 and 16, respectively. In the stress field evolution (Figs. 15a and 16a), the magnitude of stress is represented by different colors. The red indicates a large compressive stress and the dark blue indicates a small stress. The spatial distribution of microcracks can be visualized by recording the breakage of the bond in DEM model (Figs. 15b and 16b), in which the red and blue dots denote the shear and tensile microcracks, respectively.

For the axial prestress ratio of 0.2, at time T_b, the dynamic maximum principal stress is at a lower level, and the distribution is also comparatively homogeneous since the specimen reached a dynamic force equilibrium state. Some damage (both tensile and shear) distributes randomly on both loading ends due to the irregular contact surfaces between the numerical specimens and bars. At time T_f, the maximum principal stress gradually concentrates on both tips of the flaw, and both OS and CS cracks initiate from the tips. At time T_p, the compressive stress increases to the peak value, and the maximum principal stress is mainly concentrated on the two OS crack regions. The microcracks coalesce and the OS cracks further propagate to the root of the specimen forming the main cracks, but the CS cracks barely develop. At time T_e, the maximum principal stress declines to a small value due to finally

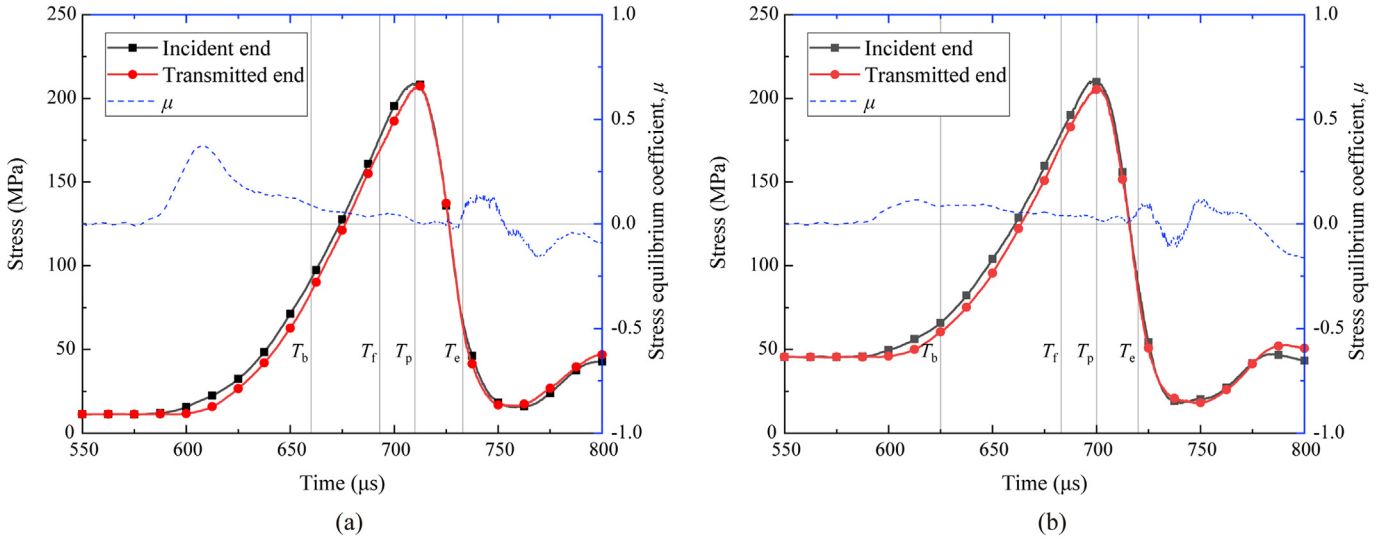

Fig. 13. Dynamic stress equilibrium check under the strain rete of 160 s^{-1} and the axial prestress ratio of (a) 0.2 and (b) 0.8.

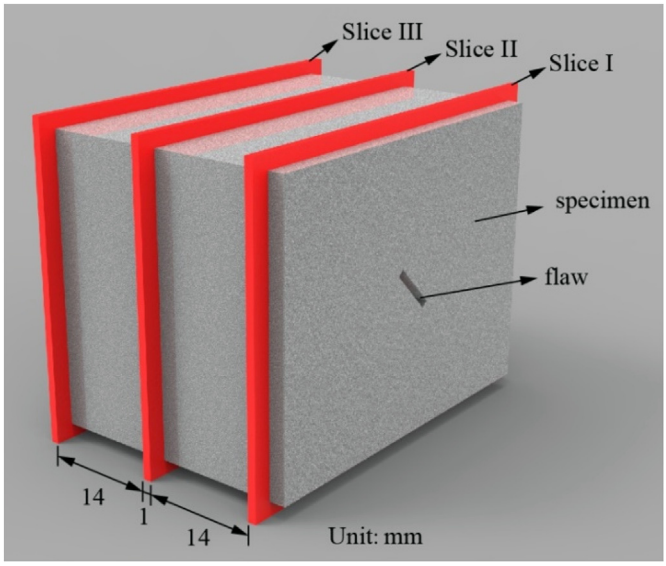

Fig. 14. Schematic diagram of the location of slices I–III for the demonstration of stress evolution and progressive cracking process.

failure of the specimen, and the OS cracks coalesce with the FS cracks eventually forming a macroscopic diagonal crack.

For the axial prestress ratio of 0.8, at time T_b, the maximum principal stress distribution is mainly marked with the same color, further showing that the specimen reached a dynamic force equilibrium state. At time T_f, stress concentrations at flaw tips are intensified, and many microcracks occur around the flaw tips. At time T_p, the maximum principal stress is concentrated on two diagonal regions of the numerical specimen. Not only OS cracks but also CS cracks develop from the flaw tips to the roots of the specimen. At time T_e, the OS and CS cracks finally coalesce with the root FS cracks, and the specimen exhibits an "X" shaped conjugated failure pattern. There are more red dots in the damage region of the specimen, indicating that the shear failure more easily occurs in the specimen.

From the above analysis, although both the CS and OS cracks initiate when the dynamic load reaches a high level, the maximum principal stress tends to concentrate on the direction opposite to wing crack, and only the OS cracks develop and coalesce to form a macroscopic non-coplanar shear crack under lower axial static prestress. Under higher axial prestress, the stress concentration is more obvious in the two diagonal directions, and the CS and OS cracks develop simultaneously, which makes the specimen present macroscopic "X" shaped conjugated failure mode.

4.3. Displacement field distribution and cracking mechanisms

Although the effect of the axial prestress on the failure pattern and cracking process of the confined single-flawed specimen has been discussed in previous sections, the cracking mechanism is not well understood. To better identify the microscopic cracking mechanism of the single-flawed specimen, the displacement field distribution of the specimen is visualized in this section. With the radial prestress of 11.4 MPa, the displacement fields of the single-flawed specimen under different axial prestresses are shown in Fig. 17. Different magnitudes of displacement are represented by different colors, and a warmer color indicates a larger displacement. The macrocracks are plotted by black dash line and the displacement interfaces are obvious at the macrocracks. To better understand the origin of different macrocrack types, the enlarged views of typical crack coalesce types are presented along different macrocracks. The enlarged views show the displacement magnitude and direction of the particles on both sides of the macrocrack.

According to Zhang and Wong (2014), the displacement trend line (DTL) is introduced for revealing the cracking mechanism, which represents the general displacement trends on both sides of a newly developed crack. As shown in Fig. 18, The DTLs on both sides of the cracking surface are indicated by the red arrows, and the green and blue arrows represent the components perpendicular and parallel to the cracking surface, respectively. The tensile properties of the newly developed crack can be identified by comparing the direction and magnitude of the two perpendicular component vectors, and the shear crack can be identified by comparing the two parallel component vectors. Therefore, five main microscopic cracking mechanism types are summarized in our tests:

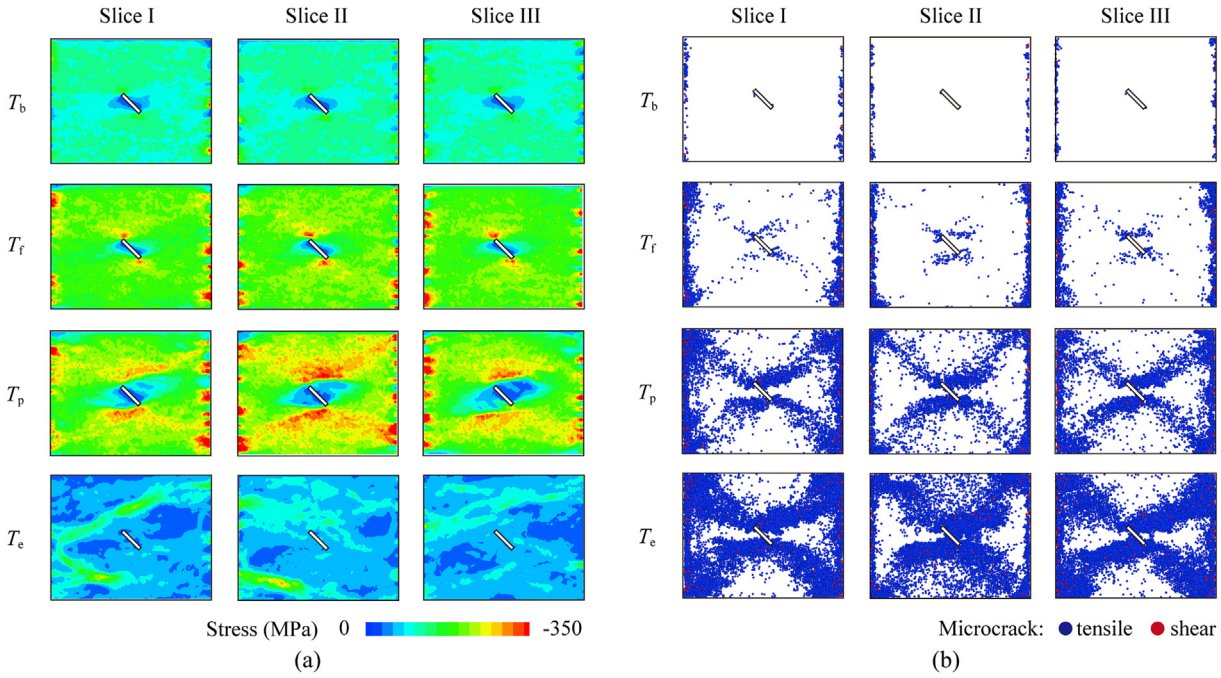

Fig. 15. (a) Dynamic maximum principal stress evolution and (b) the progressive cracking process of the single-flawed specimen at the strain rate of about 160 s^{-1} and axial prestress ratio of 0.2.

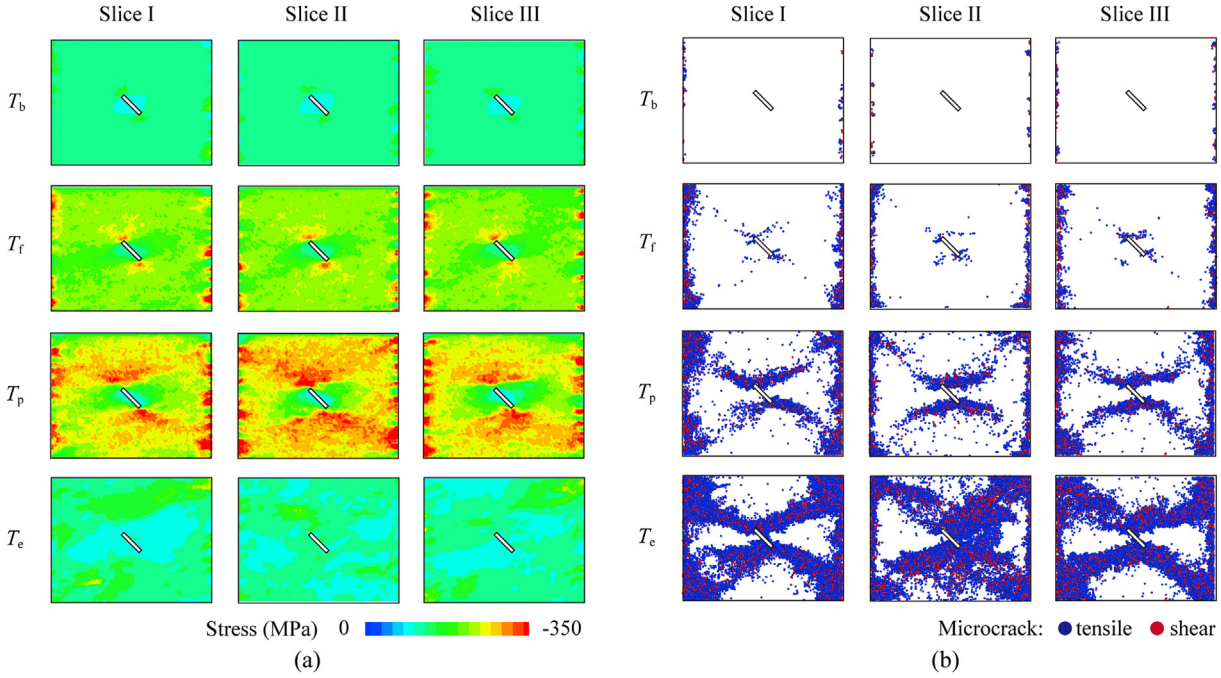

Fig. 16. (a) Dynamic maximum principal stress evolution and (b) the progressive cracking process of the single-flawed specimen at the strain rate of about 160 s^{-1} and axial prestress ratio of 0.8.

(1) Type I: Direct tensile (DT) crack. The parallel component vectors on both sides of the cracking surface are similar in magnitude and direction, while the perpendicular component vectors move in the opposite direction (Fig. 18a).
(2) Type II: Relative tensile (RT) crack. The parallel component vectors on both sides of the cracking surface are similar in magnitude and direction, while the perpendicular component vectors move in the same direction but unequal in magnitude (Fig. 18b).
(3) Type III: Relative shear (RS) crack. The perpendicular component vectors on both sides of the cracking surface are similar in magnitude and direction, while the parallel component vectors move in the same direction but unequal in magnitude (Fig. 18c).

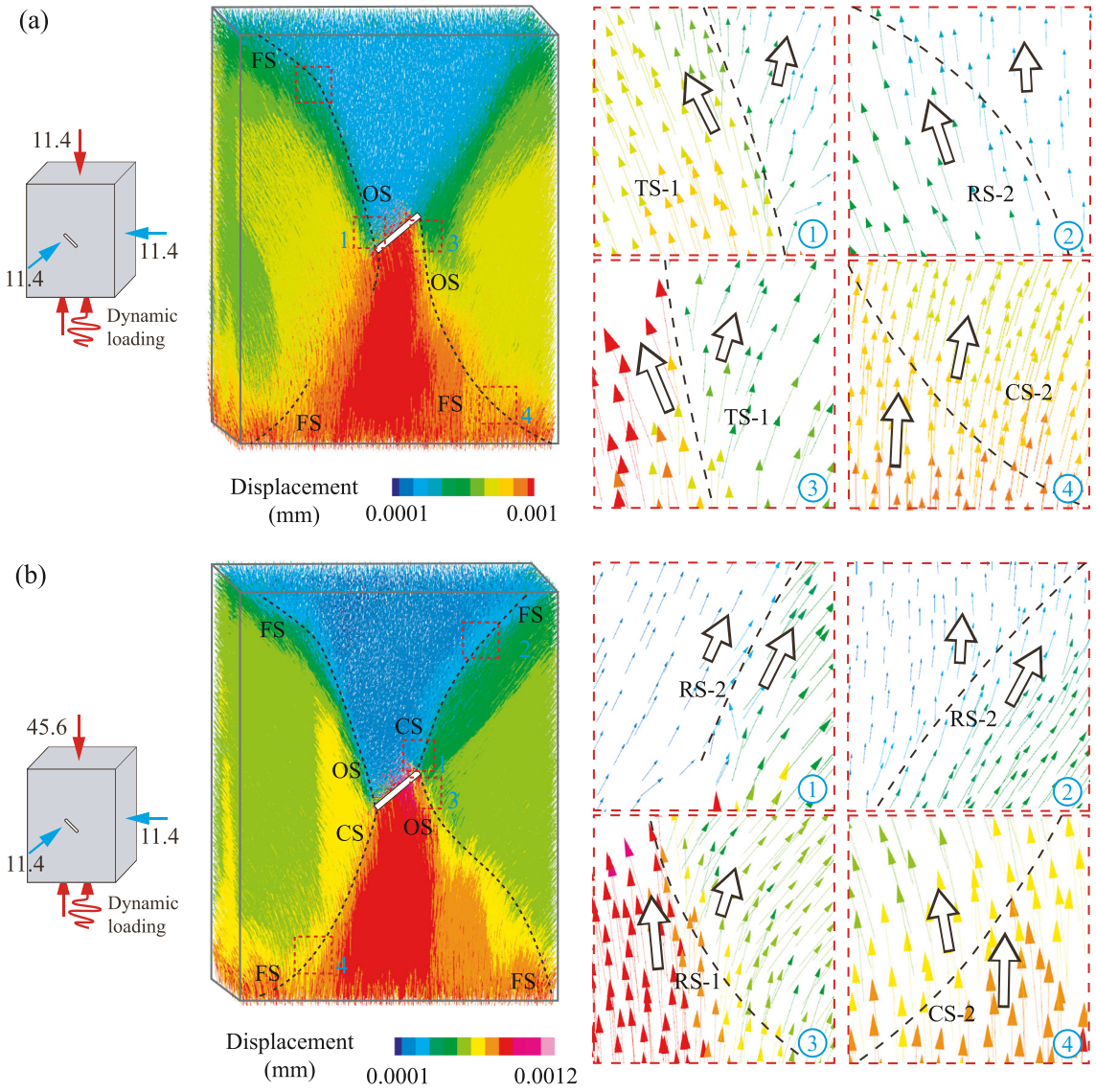

Fig. 17. Displacement field distribution of confined single-flawed specimen under the axial prestress ratios of (a) 0.2 and (b) 0.8. Narrow solid arrows and thick open arrows represent the displacement vectors and DTLs, respectively.

(4) Type IV: Tensile-shear (TS) crack. The parallel component vectors on both sides of the cracking surface move in the same direction but unequal in magnitude. The relative motion between perpendicular component vectors is separating from each other (Fig. 18d).
(5) Type V: Compression-shear (CS) crack. The parallel component vectors on both sides of the cracking surface move in the same direction but unequal in magnitude. The relative motion between perpendicular component vectors is approaching each other (Fig. 18e).

Generally, a DT or RT crack leads to a tensile crack, while RS, TS or CS crack will cause a shear crack. Based on the enlarged views shown in Fig. 17a, we can find that the diagonal macroscopic OS cracks at the flaw tips are actually mixed tensile-shear cracks dominated by TS cracks. The macroscopic FS cracks near the root region of the specimen are shear cracks characterized by RS or CS cracks. The results indicate that a macroscopic diagonal failure at lower axial prestress is mainly controlled by mixed tensile-shear cracks. Under a higher axial prestress ratio of 0.8, the macroscopic OS and CS cracks initiating at the flaw tips are shear cracks mainly controlled by RS cracks, while the macroscopic FS cracks are also shear cracks characterized by RS or CS cracks, as shown in Fig. 17b. Therefore, the "X" shaped conjugated failure for higher axial prestress is shear dominated. In the DEM simulation, most of the cracks, especially the FS cracks, are shear cracks, while tensile cracks (DT and RT) are hardly observed, which is highly consistent with the experimental results of the confined single-flawed specimen in coupled static-dynamic tests.

5. Conclusions

In this study, to simulate the fractured rock confronted with 3D in situ stress and dynamic disturbance simultaneously, the triaxial SHPB tests are experimentally and numerically conducted on single-flawed rocks. Our experimental results reveal the influences of axial prestress and strain rate on the dynamic mechanical response of confined single-flawed rocks, and the numerical results provide further insights into the progressive fracture process and

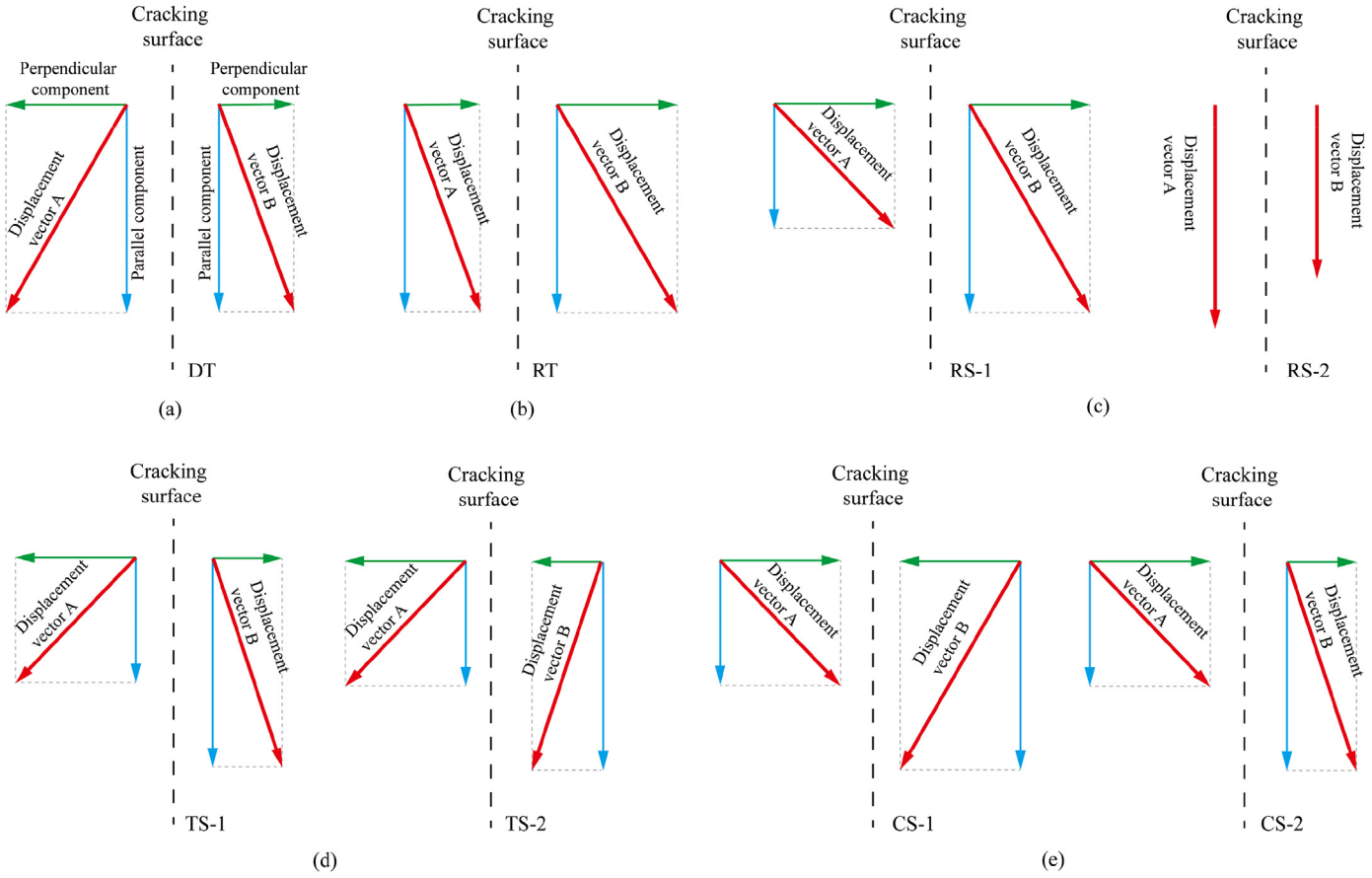

Fig. 18. Five displacement field types defined by DTLs: (a) DT, (b) RT, (c) RS, (d) TS, and (e) CS.

cracking mechanism. The following main conclusions can be drawn:

(1) Both the dynamic strength and total strength of single-flawed rocks show significant positive linear correlations with the strain rate, and strain rate sensitivity of dynamic strength is more obvious under higher axial prestress. The dynamic strength and corresponding failure strain decrease with increasing axial prestress, while the total strength is barely affected by the axial prestress. The dynamic elastic modulus first increases and then decreases at a turning point, i.e. the axial prestress ratio about 0.6.

(2) The axial prestress significantly affects the failure pattern of the confined single-flawed specimen under coupled static-dynamic loading. Under lower axial prestress (i.e. the prestress ratio of 0.2), rocks generally exhibit a macroscopic diagonal failure pattern and are broken into two major fragments. Under higher axial prestress (i.e. the prestress ratio between 0.4 and 0.8), the failure pattern converts into an "X" shaped conjugated failure mode, and four major fragments are usually formed after failure.

(3) The dynamic stress field evolution and the displacement field distributions of confined single-flawed rocks are numerically visualized, and five main microscopic cracking mechanism types are identified and classified in our simulation based on DTLs on both sides of the cracking surface. The displacement field distributions of the DEM models reveal that the macroscopic single diagonal failure under lower axial prestress is mainly controlled by mixed tensile-shear cracks, while the "X" shaped conjugated failure under higher axial prestress is shear dominated.

Declaration of competing interest

The authors declare that they have no known competing financial interests or personal relationships that could have appeared to influence the work reported in this paper.

Acknowledgments

The authors are grateful for the financial support from the National Natural Science Foundation of China (Grant Nos. 52039007 and 52009086), and the Youth Science and Technology Innovation Team of Sichuan Province, China (Grant No. 2020JDTD0001).

References

Bobet, A., Einstein, H.H., 1998. Fracture coalescence in rock-type materials under uniaxial and biaxial compression. Int. J. Rock Mech. Min. Sci. 35 (7), 863–888.
Chen, R., Yao, W., Lu, F., Xia, K., 2018. Evaluation of the stress equilibrium condition in axially constrained triaxial SHPB tests. Exp. Mech. 58 (3), 527–531.
Dai, F., Huang, S., Xia, K.W., Tan, Z.Y., 2010. Some fundamental issues in dynamic compression and tension tests of rocks using split Hopkinson pressure bar. Rock Mech. Rock Eng. 43 (6), 657–666.
Ding, X.B., Zhang, L.Y., Zhu, H.H., Zhang, Q., 2014. Effect of model scale and particle size distribution on PFC3D simulation results. Rock Mech. Rock Eng. 47 (6), 2139–2156.
Du, H.B., Dai, F., Liu, Y., Xu, Y., Wei, M.D., 2020a. Dynamic response and failure mechanism of hydrostatically pressurized rocks subjected to high loading rate impacting. Soil Dynam. Earthq. Eng. 129, 105927.

Du, H.B., Dai, F., Xu, Y., Yan, Z., Wei, M.D., 2020b. Mechanical responses and failure mechanism of hydrostatically pressurized rocks under combined compression-shear impacting. Int. J. Mech. Sci. 165, 105219.
Feng, P., Dai, F., Liu, Y., Xu, N.W., Zhao, T., 2018. Effects of strain rate on the mechanical and fracturing behaviors of rock-like specimens containing two unparallel fissures under uniaxial compression. Soil Dynam. Earthq. Eng. 110, 195–211.
Frew, D.J., Forrestal, M.J., Chen, W., 2001. A split Hopkinson pressure bar technique to determine compressive stress-strain data for rock materials. Exp. Mech. 41 (1), 40–46.
Gong, F.Q., Si, X.F., Li, X.B., Wang, S.Y., 2019. Dynamic triaxial compression tests on sandstone at high strain rates and low confining pressures with split Hopkinson pressure bar. Int. J. Rock Mech. Min. Sci. 113, 211–219.
Hokka, M., Black, J., Tkalich, D., et al., 2016. Effects of strain rate and confining pressure on the compressive behavior of Kuru granite. Int. J. Impact Eng. 91, 183–193.
Huang, C., Yang, W., Duan, K., Fang, L., Wang, L., Bo, C., 2019. Mechanical behaviors of the brittle rock-like specimens with multi-non-persistent joints under uniaxial compression. Construct. Build. Mater. 220, 426–443.
Huang, D., Gu, D.M., Yang, C., Huang, R.Q., Fu, G.Y., 2016a. Investigation on mechanical behaviors of sandstone with two preexisting flaws under triaxial compression. Rock Mech. Rock Eng. 49 (2), 375–399.
Huang, Y.H., Yang, S.Q., Zhao, J., 2016b. Three-dimensional numerical simulation on triaxial failure mechanical behavior of rock-like specimen containing two unparallel fissures. Rock Mech. Rock Eng. 49 (12), 4711–4729.
Jiang, R., Dai, F., Liu, Y., Li, A., 2021. Fast marching method for microseismic source location in cavern-containing rockmass: performance analysis and engineering application. Engineering 7 (7), 1023–1034.
Kolsky, H., 1949. An investigation of the mechanical properties of materials at very high rates of loading. Proc. Phys. Soc. B 62 (11), 676–700.
Lee, H., Jeon, S., 2011. An experimental and numerical study of fracture coalescence in pre-cracked specimens under uniaxial compression. Int. J. Solid Struct. 48 (6), 979–999.
Li, A., Dai, F., Liu, Y., Du, H., Jiang, R., 2021. Dynamic stability evaluation of underground cavern sidewalls against flexural toppling considering excavation-induced damage. Tunn. Undergr. Space Technol. 112, 103903.
Li, D.Y., Han, Z.Y., Sun, X.L., Zhou, T., Li, X.B., 2019. Dynamic mechanical properties and fracturing behavior of marble specimens containing single and double flaws in SHPB tests. Rock Mech. Rock Eng. 52 (6), 1623–1643.
Li, X., Zhou, Z., Lok, T.S., Hong, L., Yin, T., 2008. Innovative testing technique of rock subjected to coupled static and dynamic loads. Int. J. Rock Mech. Min. Sci. 45 (5), 739–748.
Li, X.B., Gong, F.Q., Tao, M., Dong, L.J., Du, K., Ma, C.D., Zhou, Z.L., Yin, T.B., 2017a. Failure mechanism and coupled static-dynamic loading theory in deep hard rock mining: a review. J. Rock Mech. Geotech. Eng. 9 (4), 767–782.
Li, X.B., Zhou, T., Li, D.Y., 2017b. Dynamic strength and fracturing behavior of single-flawed prismatic marble specimens under impact loading with a split-Hopkinson pressure bar. Rock Mech. Rock Eng. 50 (1), 29–44.
Li, Y.P., Chen, L.Z., Wang, Y.H., 2005. Experimental research on pre-cracked marble under compression. Int. J. Solid Struct. 42 (9–10), 2505–2516.
Liu, Y., Dai, F., Zhao, T., Xu, N.W., 2017. Numerical investigation of the dynamic properties of intermittent jointed rock models subjected to cyclic uniaxial compression. Rock Mech. Rock Eng. 50 (1), 89–112.
Liu, Y., Dai, F., 2021. A review of experimental and theoretical research on the deformation and failure behavior of rocks under cyclic loads. J. Rock Mech. Geotech. Eng. 13 (5), 1203–1230.
Liu, Y., Dai, F., Pei, P., 2021. A wing-crack extension model for tensile response of saturated rocks under coupled static-dynamic loading. Int. J. Rock Mech. Min. Sci. 146, 104893.
Pei, P.D., Dai, F., Liu, Y., Wei, M.D., 2020. Dynamic tensile behavior of rocks under static pre-tension using the flattened Brazilian disc method. Int. J. Rock Mech. Min. Sci. 126, 104208.
Potyondy, D.O., Cundall, P.A., 2004. A bonded-particle model for rock. Int. J. Rock Mech. Min. Sci. 41 (8), 1329–1364.
Sagong, M., Bobet, A., 2002. Coalescence of multiple flaws in a rock-model material in uniaxial compression. Int. J. Rock Mech. Min. Sci. 39 (2), 229–241.
Shaunik, D., Singh, M., 2019. Strength behaviour of a model rock intersected by non-persistent joint. J. Rock Mech. Geotech. Eng. 11 (6), 1243–1255.
Tang, J.Z., Yang, S.Q., Tian, W.L., Tao, Y., 2019. Effect of confining pressure on mechanics and deformation behavior of sandstone containing a single inclined joint. Eur. J. Environ. Civ. Eng. 1–24.
Weatherley, D., Hancock, W., Boris, V., 2014. ESyS-particle tutorial and user's guide version 2.1. Earth Systems Science Computational Centre. The University of Queensland.
Wei, M., Dai, F., Liu, Y., Li, A., Yan, Z., 2021. Influences of loading method and notch type on rock fracture toughness measurements: from the perspectives of T-stress and fracture process zone. Rock Mech. Rock Eng. 54 (9), 4965–4986.
Wong, R.H.C., Chau, K.T., 1998. Crack coalescence in a rock-like material containing two cracks. Int. J. Rock Mech. Min. Sci. 35 (2), 147–164.
Wu, B.B., Chen, R., Xia, K.W., 2015. Dynamic tensile failure of rocks under static pre-tension. Int. J. Rock Mech. Min. Sci. 80, 12–18.
Xia, K.W., Yao, W., 2015. Dynamic rock tests using split Hopkinson (Kolsky) bar system - a review. J. Rock Mech. Geotech. Eng. 7 (1), 27–59.
Xiao, P., Li, D.Y., Zhao, G.Y., Zhu, Q.Q., Liu, H.X., Zhang, C.S., 2020. Mechanical properties and failure behavior of rock with different flaw inclinations under coupled static and dynamic loads. J. Cent. South Univ. 27 (10), 2945–2958.
Xu, Y., Dai, F., Xu, N.W., Zhao, T., 2016. Numerical investigation of dynamic rock fracture toughness determination using a semi-circular bend specimen in split Hopkinson pressure bar testing. Rock Mech. Rock Eng. 49 (3), 731–745.
Xu, Y., Dai, F., Du, H.B., 2020. Experimental and numerical studies on compression-shear behaviors of brittle rocks subjected to combined static-dynamic loading. Int. J. Mech. Sci. 175, 105520.
Yan, Z.L., Dai, F., Liu, Y., Du, H.B., Luo, J., 2020. Dynamic strength and cracking behaviors of single-flawed rock subjected to coupled static-dynamic compression. Rock Mech. Rock Eng. 53 (9), 4289–4298.
Yan, Z.L., Dai, F., Liu, Y., Li, Y.Z., You, W., 2021. Experimental investigation of pre-flawed rocks under combined static-dynamic loading: mechanical responses and fracturing characteristics. Int. J. Mech. Sci. 211, 106755.
You, W., Dai, F., Liu, Y., Du, H.B., Jiang, R.C., 2021. Investigation of the influence of intermediate principal stress on the dynamic responses of rocks subjected to true triaxial stress state. Int. J. Min. Sci. Technol. 31 (5), 913–926.
Zhang, X.P., Wong, L.N.Y., 2014. Displacement field analysis for cracking processes in bonded-particle model. Bull. Eng. Geol. Environ. 73 (1), 13–21.
Zhao, J., Zhou, Y.X., Hefny, A.M., Cai, J.G., Chen, S.G., Li, H.B., Liu, J.F., Jain, M., Foo, S.T., Seah, C.C., 1999. Rock dynamics research related to cavern development for ammunition storage. Tunn. Undergr. Space Technol. 14 (4), 513–526.
Zhou, Y.X., Xia, K., Li, X.B., Li, H.B., Ma, G.W., Zhao, J., Zhou, Z.L., Dai, F., 2012. Suggested methods for determining the dynamic strength parameters and mode-I fracture toughness of rock materials. Int. J. Rock Mech. Min. Sci. 49, 105–112.
Zou, C.J., Wong, L.N.Y., 2014. Experimental studies on cracking processes and failure in marble under dynamic loading. Eng. Geol. 173, 19–31.

Feng Dai obtained his BSc and MSc degrees from Sichuan University, and PhD degree from University of Toronto, Canada. He is currently a professor at Sichuan University and has been appointed as a member of the 8th Science and Technology Commission of the Ministry of Education, China. He has long-time research experiences on rock dynamics and rock engineering and has been in charge of more than 20 research projects, including Major Program of National Natural Science Foundation of China, 973 project, etc. He has published 187 research papers with citations more than 4500 times in Scopus. Since 2018, he had been enrolled as Elsevier Most Cited Chinese Researcher. He has received multiple awards including First Prize Award of Science & Technology Achievement of Ministry of Education, China (ranked No. 1). He has been an Associate Editor of *International Journal of Geomechanics* and a member of editorial board for other seven international journals.